INORGANIC CHEMISTRY FRONTIERS

RESEARCH ARTICLE

View Article Online
View Journal

Cite this: DOI: 10.1039/d5qi00437c

Boosting hydrogen evolution and triiodide reduction *via* electronic coupling on a (1T, 2H) MoS_2@N-doped carbon dodecahedron†

Lan Yu,‡[a] Chengxu Liu,‡[a] Li Sun,[a] Wei Kan,[a] Ying Xie,[b] Xiuwen Wang,*[a] Yuying Cao,[a] Bing Zhao*[a] and Chunmei Lv*[a]

Received 13th February 2025,
Accepted 8th April 2025

DOI: 10.1039/d5qi00437c

rsc.li/frontiers-inorganic

Designing a noble-metal-free catalyst with the desired composition and structure is highly significant for accelerating the catalytic kinetics of the hydrogen evolution reaction (HER) and triiodide reduction reaction (IRR), which is essential for advancing green hydrogen production from water electrolysis and improving the power conversion efficiency (PCE) of dye-sensitized solar cells (DSSCs). Herein, small-sized (1T, 2H) phase MoS_2 nanosheets were uniformly wrapped around an N-doped C dodecahedron (MoS_2@NC) through a continuous synthesis strategy with ZIF-8 serving as the original template. When MoS_2@NC is used as a catalyst for the HER, it only requires a low overpotential of 93 mV to reach 10 mA cm^{-2}, surpassing most reported MoS_2-based catalysts. Furthermore, a device fabricated with MoS_2@NC achieves a PCE of 8.20%, which is comparable to that of a Pt-based one (8.59%). Theoretical calculations revealed that the enhanced HER activity of MoS_2@NC is mainly attributed to the enhanced water adsorption energy and a reduced energy barrier for overcoming the rate-determining step during the HER process. Additionally, the interfacial S sites in MoS_2@NC are responsible for the excellent catalytic activity in the IRR. The experimental and theoretical results collectively confirm that the as-designed MoS_2@NC is a promising bifunctional catalyst.

1. Introduction

The development of sustainable energy sources, such as hydrogen and solar energy, plays a vital role in addressing global energy shortages and increasing environmental pollution.[1–4] Hydrogen production through the cathode hydrogen evolution reaction (HER) in alkaline water electrolysis and solar energy conversion *via* dye-sensitized solar cells (DSSCs) are two promising and viable technologies for advancing cleaner energy.[5–8] Nevertheless, the efficiency of both processes is fundamentally restricted by the thermodynamically uphill reactions. In particular, the HER in water electrolysis and the triiodide reduction reaction (IRR) involved in DSSCs are key factors that determine the overall performance of electrocatalytic water splitting and DSSCs, respectively.[9–12] Traditionally, the benchmark catalysts for both the HER and IRR have highly relied on noble-metal-based catalysts,[13–16] but their scarcity and high cost pose significant challenges for the large-scale implementation and commercialization of these technologies.[17–20] Therefore, there is an urgent demand to develop cost-effective, scalable, and high-performance bifunctional catalysts that can efficiently accelerate HER and IRR processes, as well as alternatives to replace precious metal-based catalysts.

Molybdenum disulfide (MoS_2), a representative transition metal dichalcogenide, has emerged as a highly promising candidate in the field of energy conversion.[21–23] The 1T and 2H phases are two main crystalline phases of MoS_2. 1T-phase MoS_2 is metallic in nature, featuring a larger interlayer distance and a high density of active sites, which makes it particularly effective in catalysing the HER and IRR.[24–26] 2H-phase MoS_2 exhibits semiconductor-like characteristics and offers remarkable durability, which is essential for maintaining long-term catalytic performance.[27,28] A promising strategy to optimize the performance of MoS_2 is to construct 1T/2H MoS_2 mixtures. It not only exploits the high catalytic activity of the 1T phase, but also takes advantage of the exceptional stability of the 2H phase, achieving a synergistic balance between catalytic activity and stability. Beyond phase manipulation, the size and

[a]*Heilongjiang Province Key Laboratory of Surface Active Agent and Auxiliary, College of Chemistry and Chemistry Engineering, Qiqihar University, Qiqihar, 161006, China. E-mail: xwwang@qqhru.edu.cn, zhao_submit@aliyun.com, 03291@qqhru.edu.cn*

[b]*Key Laboratory of Functional Inorganic Material Chemistry, Ministry of Education, Heilongjiang University, Harbin, 150080, China*

†Electronic supplementary information (ESI) available. See DOI: https://doi.org/10.1039/d5qi00437c

‡These authors contributed equally to this work.

morphology of MoS_2 constitute another factor in determining its catalytic efficiency. Studies have shown that the edge active sites of MoS_2 nanosheets play a pivotal role in boosting catalytic performance, as they provide unsaturated bonds and active sites that enhance catalytic activity.[29–31] However, MoS_2 at the nanoscale tends to undergo aggregation, resulting in a reduced effective surface area and compromised catalytic performance. To address this limitation, uniformly dispersing small-sized MoS_2 nanosheets on a carbon-based support can effectively prevent their aggregation and facilitate synergy. Therefore, elaborately designing the phase composition of MoS_2, optimizing its nanostructure, and integrating it with carbon-based materials, can significantly enhance its catalytic activity and structural stability. These advancements are key to the development of cost-effective and scalable catalysts, positioning MoS_2-based composites as a highly promising solution for energy conversion applications.

Zeolitic imidazolate frameworks (ZIF-8) have gained considerable attention because of their distinctive structure and capacity to act as templates for the synthesis of functional catalysts.[32,33] In particular, ZIF-8 derived carbon-based materials, with a well-defined structure, can serve as an appropriate substrate for the *in situ* growth of active species such as MoS_2. The templating method using carbon-based materials derived from ZIF-8 allows for precise control over the morphology and distribution of MoS_2 nanosheets, ensuring that the resulting composites deliver optimal performance and potential in electrocatalytic applications such as the HER and IRR.

In this work, we present a continuous synthesis approach to uniformly synthesize 1T, 2H-MoS_2 nanosheets wrapped around a nitrogen-doped carbon dodecahedron (MoS_2@NC), with ZIF-8 serving as the original template. Not only does it fully leverage the synergistic component advantages between the 1T and 2H phases of MoS_2 and NC, but the well-preserved dodecahedral structure also provides a stable framework that ensures the effective exposure of edge-active sites on the small-sized MoS_2 nanosheets, endowing MoS_2@NC with remarkable catalytic activity for both the HER and IRR. Specifically, the optimized MoS_2@NC exhibits a low overpotential of 93 mV at a current density of 10 mA cm^{-2}, surpassing most of the reported MoS_2-based HER catalysts in 1.0 M KOH. Furthermore, a PCE of 8.20% was delivered when the obtained MoS_2@NC was employed as a counter electrode (CE) catalyst for DSSCs, which is comparable to that of the Pt-based device (8.59%). The enhanced HER activity of MoS_2@NC can be attributed to the accelerated HER kinetics resulting from the further enhanced water adsorption energy and lowered energy barrier for overcoming the rate-determining step (RDS) compared to that of MoS_2, and the excellent catalytic activity of MoS_2@NC for the IRR mainly stems from the interfacial S sites (I_3^- preferentially adsorbs at the interfacial S sites, the covalent bond between S and I_1 of I_3^-, and the strong interaction between S 3p and I 5p). Therefore, the as-designed MoS_2@NC is a promising bifunctional catalyst for both the HER and IRR.

2. Experimental section

2.1 Synthesis of ZIF-8

30.0 g of 2-methylimidazole was dissolved in 200 mL of deionized water to form a clear solution. In another separate beaker, 7.2 g of $Zn(CH_3COO)_2{\cdot}2H_2O$ was fully dissolved in 200 mL of deionized water to obtain a homogeneous solution. After mixing the two mentioned solutions, the resulting mixture was left at room temperature for 48 h, during which the white precipitate could be collected. Afterward, this precipitate was washed several times with deionized water to remove impurities and then dried at 60 °C for 8 h to yield ZIF-8.

2.2 Preparation of Z-NC

Fresh ZIF-8 was placed at the center of a tube furnace and subjected to carbonization under a nitrogen atmosphere at 800 °C for 1 h with a heating rate of 5 °C min^{-1}. After cooling down to 25 °C, the resulting dodecahedral N-doped carbon containing zinc was denoted as Z-NC.

2.3 Synthesis of NC

To remove the zinc incorporated in NC, the obtained NC was washed with HCI (35%) several times. Then the collected samples were further rinsed with deionized water to eliminate any remaining and then dried at 60 °C for 8 h. The obtained product was designated as NC.

2.4 Synthesis of MoS_2@NC

50.0 mg of NC was initially dispersed in 25 mL of 0.05 M glucose solution to obtain a homogeneous solution. Subsequently, 1.2 mmol $Na_2MoO_4{\cdot}2H_2O$ and 7.9 mmol thiourea were successively added to the mixture. After stirring for 30 min, the mixture was transferred to a 50 mL autoclave and heated to 200 °C for 24 h. Upon cooling to room temperature, the black precipitate was collected by centrifugation and thoroughly washed with deionized water several times, followed by drying at 60 °C. The obtained sample was labelled as MoS_2@NC.

2.5 Preparation of MoS_2, MoS_2@NC-1, and MoS_2@NC-3

The preparation of MoS_2 was similar to that of the above MoS_2@NC, except without adding NC. The preparation of MoS_2@NC-1 and MoS_2@NC-3 was also similar to that of MoS_2@NC, except that the molar mass of $Na_2MoO_4{\cdot}2H_2O$ changed to 1.0 and 1.4 mmol, respectively.

3. Results and discussion

3.1 Materials synthesis and characterization

The preparation of (1T, 2H) MoS_2@NC composites (denoted as MoS_2@NC) involves four critical steps: coprecipitation, carbonization, acid washing, and the hydrothermal method (Fig. 1a). Initially, dodecahedral ZIF-8 with uniform size was synthesized through a simple precipitation approach (Fig. 1b). ZIF-8 was

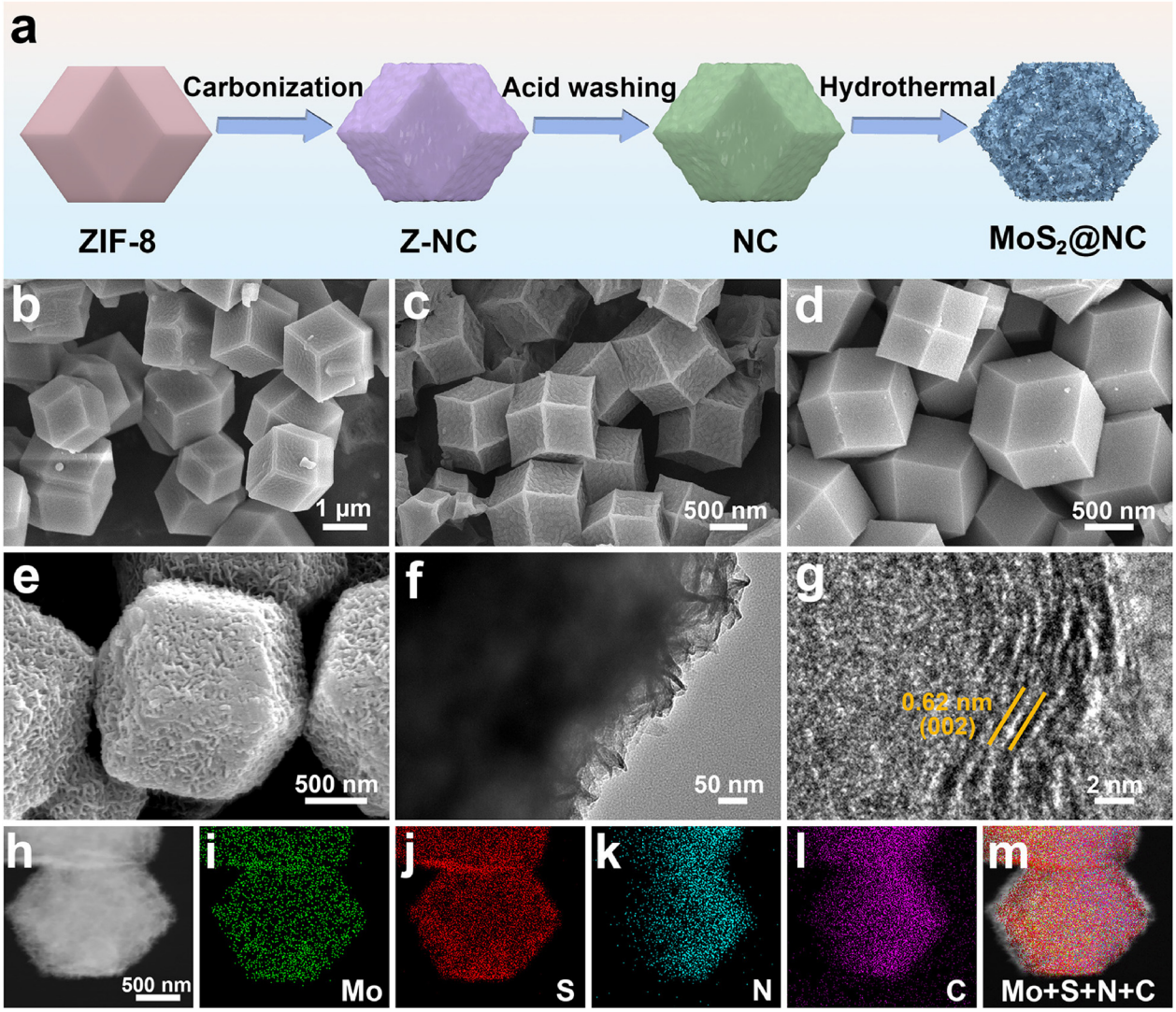

Fig. 1 (a) Schematic diagram of the synthesis of MoS_2@NC. SEM images of (b) ZIF-8, (c) Z-NC, (d) NC, and (e) MoS_2@NC. (f) TEM, (g) HRTEM, and (h–m) elemental mapping images of MoS_2@NC.

then pyrolyzed at 800 °C under a nitrogen atmosphere for 1 h using a carbonization method, resulting in the formation of dodecahedral Z-NC containing zinc with a rough surface (Fig. 1c). Subsequently, Zn-free NC (NC) can be synthesized by acid washing with a controlled amount of HCl (Fig. 1d). Finally, small-sized (1T, 2H) MoS_2 nanosheets were uniformly wrapped around the NC surface to generate well-defined MoS_2@NC dodecahedron composites through a hydrothermal method (Fig. 1e). The abundant folds in the small-sized MoS_2 nanosheets notably increase the specific surface area, thereby promoting the availability of edge active sites for reactant molecules. Meanwhile, the conductive NC component improves the overall electrical conductivity, facilitating faster charge transfer at the interface. The positive synergy between (1T, 2H) MoS_2 and NC accelerates catalytic kinetics and leads to remarkable performance. Transmission electron microscopy (TEM) in Fig. 1f further revealed that MoS_2 nanosheets were well stacked onto the NC dodecahedron surface. The high-resolution TEM (HRTEM) image confirmed that the distinct lattice fringes at the edge correspond to the MoS_2 (002) plane (Fig. 1g),[25,34] providing clear evidence for the successful preparation of MoS_2 covered on the NC surface. The elemental mapping images (Fig. 1h–m) suggested a uniform distribution of Mo, S, N, and C elements throughout the entire region, meaning that the MoS_2 nanosheets are evenly wrapped around the NC dodecahedron surface. Furthermore, the counterparts of MoS_2, MoS_2@NC-1, and MoS_2@NC-3 were also synthesized through a similar approach. As depicted in Fig. S1a and b,† only MoS_2 aggregation can be found, highlighting the crucial role of NC in preparing MoS_2@NC. While MoS_2@NC-1 and MoS_2@NC-3 retain the dodecahedron morphology (Fig. S1c–f†), MoS_2@NC-3, in particular, shows an increase in the amount of $Na_2MoO_4{\cdot}2H_2O$, which led to significant aggregation on the NC surface, revealing that an appropriate amount of $Na_2MoO_4{\cdot}2H_2O$ is necessary.

Raman spectroscopy was used to characterize the phase composition of as-synthesized samples. As depicted in Fig. 2a, the characteristic peaks at 147, 196, and 337 cm^{-1} belong to the J_1 and J_2, J_3 modes of the 1T phase of MoS_2 (1T-MoS_2), while the Raman peaks at 282 and 380 cm^{-1} are ascribed to the E_{1g} and E_{2g} of the 2H phase of MoS_2 (2H-MoS_2), which collectively verify the coexistence of 1T-MoS_2 and 2H-MoS_2 in MoS_2@NC composites. Meanwhile, the D and G bands of NC were also observed at 1380 cm^{-1} and 1571 cm^{-1}, where the D band indicates defects or disorder within the graphene structure, while the G band is related to the in-plane vibration of carbon atoms in graphitic materials. For bare MoS_2, only the J_2 and J_3 modes of 1T-MoS_2 and E_{1g} of 2H-MoS_2 are observed in Fig. 2b, implying the obtained MoS_2 composed of 1T-MoS_2 and 2H-MoS_2. The typical D and G bands in Fig. 2c represent the successful preparation of NC. For MoS_2@NC-1 and MoS_2@NC-3 (Fig. S2†), their phase composition was analogous to that of MoS_2@NC, demonstrating that the as-designed synthesis strategy is a reliable route for preparing (1T, 2H) MoS_2@NC composites.

X-ray photoelectron spectroscopy (XPS) was performed to investigate the surface chemical states of MoS_2@NC. XPS survey spectrum in Fig. 2d shows the presence of Mo, S, N, C, and O elements in MoS_2@NC. The Mo 3d XPS spectrum (Fig. 2e) displays two pairs of peaks at 228.5 eV/232.0 eV and 228.9 eV/232.7 eV, which are assigned to the Mo^{4+} $3d_{5/2}$/Mo^{4+} $3d_{3/2}$ of 1T-MoS_2 and 2H-MoS_2, respectively, indicating the coexistence of 1T-phase MoS_2 and 2H-phase MoS_2 in obtained MoS_2@NC.[21,24,25,35] Additionally, two peaks located at 225.6 eV and 235.7 eV correspond to S 2s and Mo^{6+}, respectively.[36,37] The high-resolution XPS spectrum of S 2p (Fig. 2f) reveals two distinct states for the S species. Namely, the S $2p_{3/2}$ and S $2p_{1/2}$ peaks at 160.7 eV/162.6 eV correspond to the S in 1T-MoS_2, while the peaks at 161.5 eV/164.1 eV are associated with S in 2H-MoS_2.[38–40] Additionally, the binding energies observed at 168.1 eV and 169.2 eV are attributed to the S–O bond and a satellite peak (Sat.) of Mo, respectively.[41,42] The N 1s spectrum in Fig. 2g shows the presence of graphitic N (401.1 eV), pyrrolic N (399.5 eV), and pyridinic N (398.0 eV), corresponding to the C–C, C–N, and C═O bonds, respectively, which fully confirmed

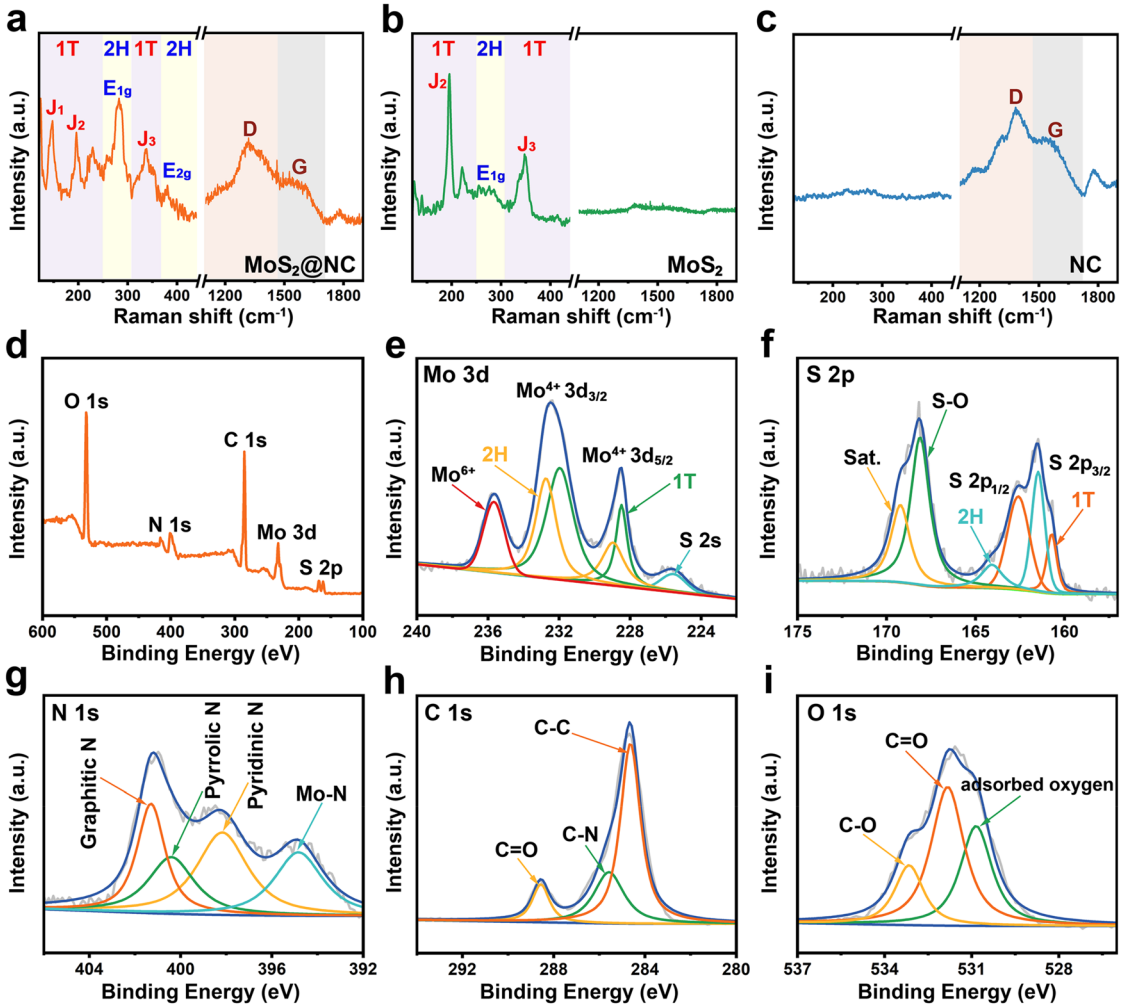

Fig. 2 Raman spectra of (a) MoS_2@NC, (b) MoS_2, and (c) NC. (d) XPS survey spectrum and high-resolution XPS spectra of (e) Mo 3d, (f) S 2p, (g) N 1s, (h) C 1s, and (i) O 1s for MoS_2@NC.

the successful doping of N into the carbon matrix.[43–45] The peak at 394.8 eV is assigned to the Mo–N. The C 1s spectrum comprises three peaks: a C–C bond at 284.9 eV, a C–N bond at 285.6 eV, and a C=O bond at 288.4 eV (Fig. 2h).[46,47] Three peaks at 531.2, 532.9, and 530.9 eV in the O 1s spectrum (Fig. 2i) respectively correspond to the C=O, C–O, and adsorbed oxygen.[48–50] These XPS results cooperatively proved that MoS_2@NC is composed of 1T-MoS_2, 2H-MoS_2 and NC.

3.2 HER performance

The HER performance of the as-prepared materials was evaluated in a 1.0 M KOH electrolyte using a three-electrode system. Linear sweep voltammetry (LSV) polarization curves in Fig. 3a indicated that the as-prepared MoS_2@NC demonstrates superior HER performance, requiring only 93, 200, and 283 mV to reach 10, 50, and 100 mA cm^{-2}, respectively. Remarkably, this performance outperforms those of MoS_2 (η_{10} = 223 mV, η_{50} = 365 mV, and η_{100} = 463 mV) and NC (η_{10} = 247 mV and η_{50} = 439 mV) (Fig. 3b), and is comparable to that of Pt/C (η_{10} = 34 mV, η_{50} = 87 mV, and η_{100} = 152 mV). The Tafel slope, extracted from the LSV curve, is utilized to evaluate the catalytic kinetic of the HER. As depicted in Fig. 3c, MoS_2@NC exhibits a Tafel slope of 98.45 mV dec^{-1}, obviously surpassing MoS_2 (183.80 mV dec^{-1}) and NC (221.99 mV dec^{-1}), indicating that MoS_2@NC undergoes a Volmer–Heyrovsky mechanism during the HER process. The impressive HER performance can be attributed to the synergy between MoS_2 and NC. Electrochemical impedance spectroscopy (EIS) was used to investigate the reaction kinetics at the catalyst/electrolyte interface. MoS_2@NC has a minimum charge transfer resistance (R_{ct}) of 2.04 Ω (Fig. 3d), which is significantly lower than that of MoS_2 (12.05 Ω) and NC (15.13 Ω), meaning that the interfacial charge transfer capability can be improved by constructing MoS_2@NC composites. Considering the merits of the chemical component and structure, the intrinsic catalytic activity of MoS_2@NC can be assessed based on the accessible

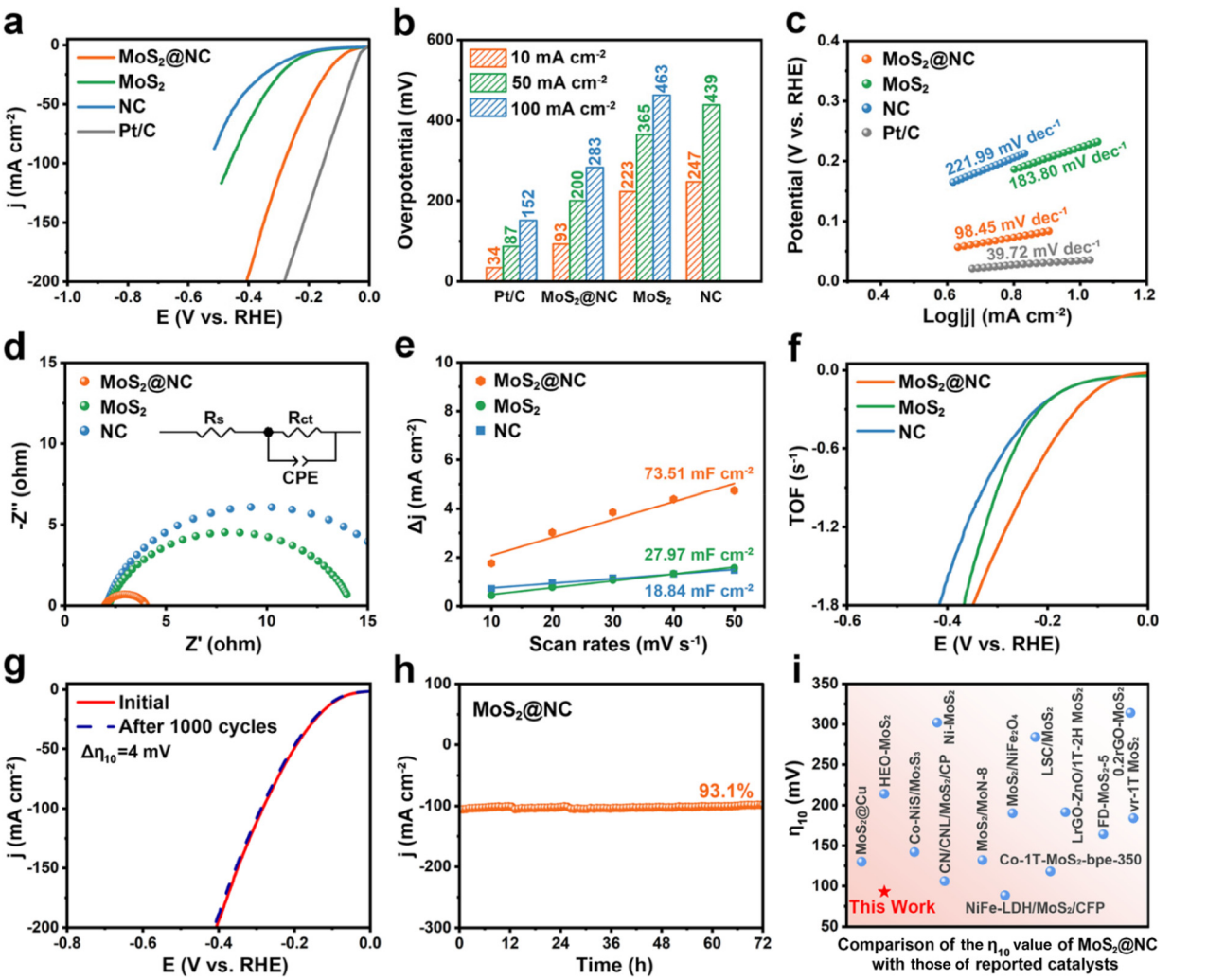

Fig. 3 HER performance of various catalysts in 1.0 M KOH: (a) LSV curves, (b) comparison of overpotentials at different current densities, (c) Tafel plots, (d) Nyquist plots, (e) C_{dl}, and (f) TOF. (g) LSV curves before and after 1000 cycles, (h) *I*–*t* curve of MoS_2@NC at 100 mA cm^{-2} for 72 h. (i) Comparison of the η_{10} value of MoS_2@NC with those of reported studies.

active sites. Electrochemical double-layer capacitance (C_{dl}) was determined from the cyclic voltammetry (CV) curves at varying scan rates within non-faradaic regions (Fig. S3†) to evaluate the electrochemical active surface areas (ECSAs). MoS_2@NC presented the largest C_{dl} value of 73.51 mF cm^{-2} (Fig. 3e), which was much larger than those of its counterparts, indicating that it has more accessible sites on the surface. The ECSA values of MoS_2@NC, MoS_2, and NC are 1838, 699, and 471 cm^{-2} (Fig. S4a†), respectively. Correspondingly, the ECSA-normalized LSV curves in Fig. S4b† indicate that MoS_2@NC has a higher j_{ecsa} value than those of MoS_2 and NC at −0.3 V. The turnover frequency (TOF) is another crucial indicator for investigating the distinct merit of electrochemical performance. In Fig. 3f, MoS_2@NC exhibits a higher TOF value of 0.613 s^{-1} at 200 mV than those of MoS_2 (0.244 s^{-1}) and NC (0.235 s^{-1}), demonstrating its superior intrinsic activity for the alkaline HER. Apart from the mentioned factors, electrochemical stability has been seen as a key criterion for evaluating the application potential. As expected, MoS_2@NC shows remarkable stability, with a slight potential loss of 4 mV after 1000 continuous CV cycles (Fig. 3g) and sustained performance over 72 h at 100 mA cm^{-2} (Fig. 3h). Subsequently, the Nyquist plots in Fig. S5† revealed that the R_{ct} value only increased by 0.02 Ω before and after the HER stability test, further demonstrating its outstanding stability. More importantly, the η_{10} value of MoS_2@NC outperforms numerous catalysts reported (Fig. 3i and Table S1†), such as CN/CNL/MoS_2/CP,[51] Co-1T-MoS_2-bpe-350,[24] MoS_2@Cu,[52] MoS_2/MoN,[53] Co-NiS/Mo_2S_3,[54] FD-MoS_2-5,[55] Ni-MoS_2,[56] vr-1T MoS_2,[57] MoS_2/$NiFe_2O_4$,[58] LrGO-ZnO/1T-2H MoS_2,[59] HEO-MoS_2,[60] LSC/MoS_2,[61] and 0.2rGO-MoS_2,[62] demonstrating exceptional HER performance.

For comparison, we also considered the effect of molybdenum disulfide loading on HER activity (Fig. S6 and S7†). The HER performance, including the overpotentials (η_{10}, η_{50}, and η_{100}), Tafel slope, R_{ct}, C_{dl}, and TOF of MoS_2@NC-1 and MoS_2@NC-3, was inferior to that of MoS_2@NC in parallel, implying that the suitable loading of MoS_2 in MoS_2@NC is an important factor in determining the overall HER performance.

3.3 Photovoltaic and IRR performance

Inspired by the excellent catalytic activity of as-constructed MoS_2@NC in the alkaline HER, employing it as a counter electrode (CE) catalyst for dye-sensitized solar cells (DSSCs) can not only explore its potential as a bifunctional catalyst but also provide a promising avenue for the replacement of precious metal platinum (Pt), which makes it a worthwhile subject of research due to its impressive application in both the renewable energy and electrocatalytic fields. Subsequently, MoS_2@NC and Pt were used as CE catalysts for iodine-based DSSCs, and their photovoltaic performance was evaluated from the photocurrent–photovoltage (J–V) curves under standard light conditions (AM1.5), as depicted in Fig. 4a and Fig. S8a.† The photovoltaic performance parameters, including power conversion efficiency (PCE), open-circuit voltage (V_{oc}), short-circuit current density (J_{sc}), and fill factor (FF), are summarized in Table S2,† based on the average values derived from six individual devices. Specifically, the PCE of DSSCs based on MoS_2@NC CE reaches 8.20% (V_{oc} = 0.739 V, J_{sc} = 16.54 mA cm^{-2}, and FF = 0.67), which is close to the performance of Pt-based ones (PCE = 8.59%, V_{oc} = 0.744 V, J_{sc} = 17.09 mA cm^{-2}, and FF = 0.68), and is superior to those of MoS_2@NC-1 (PCE = 7.72%, V_{oc} = 0.739 V, J_{sc} = 15.98 mA cm^{-2}, and FF = 0.65) and MoS_2@NC-3 (PCE = 7.07%, V_{oc} = 0.736 V, J_{sc} = 15.10 mA cm^{-2}, and FF = 0.64). More importantly, the PCE of MoS_2@NC was also higher than that of most of the reported MoS_2-based CE catalysts (Fig. 4b and Table S3†), such as MNCS-2,[63] MoS_2/rGO,[64] MoS_2@RGO,[65] MoS_2@carbon,[66] MoS_2/G,[67] CuS/MoS_2,[68] CoS/MoS_2,[69] MoS_2/graphene,[70] and MoS_2/graphene,[71] highlighting its superior performance. This improvement is likely attributed to the synergy between (1T, 2H) MoS_2 and NC, the abundant edge active sites originating from small-sized MoS_2 nanosheets at the surface, and the unique dodecahedral morphology. This suggests that the obtained MoS_2@NC holds potential as a representative non-Pt CE catalyst, offering a promising alternative for use in iodine-based electrolytes.

To evaluate the IRR activity of MoS_2@NC and Pt, cyclic voltammetry (CV) curves were first performed. In a CV curve, a larger absolute value of the reduction peak current density (I_p) and a smaller potential difference between oxidation and reduction peak (E_{pp}) values usually signify better catalytic activity and reversibility, respectively. As shown in Fig. 4c, S8b and Table S4,† MoS_2@NC has a larger I_p value (−1.77 mA cm^{-2}) compared to MoS_2@NC-1 (−1.41 mA cm^{-2}) and MoS_2@NC-3 (−1.14 mA cm^{-2}), and is very close to the benchmark of Pt (I_p = −2.09 mA cm^{-2}). This revealed that the as-synthesized MoS_2@NC has Pt-like catalytic activity for the IRR. The E_{pp} values of Pt and MoS_2@NC were 0.43 and 0.49 V, respectively, meaning the remarkable reversibility of MoS_2@NC. Moreover, the Tafel polarization curve serves as another approach to represent the catalytic activity of CE catalysts for the IRR, where the exchange current density (J_0) and the limiting diffusion current density (J_{lim}) are key indicators for evaluating the potential of CE catalysts. J_0 can be determined by the intersection of the cathodic branches with the equilibrium potential line, while J_{lim} is obtained from the intercept of the cathodic branch on the Y-axis. MoS_2@NC shows further improvements in both J_0 and J_{lim} compared to MoS_2@NC-1 and MoS_2@NC-3 (Fig. 4d, Fig. S8c and Table S4†), indicating that an appropriate amount of MoS_2 on the NC surface is beneficial for maximizing catalytic activity. The J_0 and J_{lim} values of MoS_2@NC are comparable to that of commercial Pt, showing Pt-like catalytic activity for the IRR, which aligns with the previous CV curves. Therefore, it can be concluded that MoS_2@NC exhibits Pt-like catalytic activity in iodine-based electrolytes. Next, the charge transfer kinetics of the CEs were analysed using Nyquist plots. The series resistance (R_s) and charge transfer resistance (R_{ct}) were extracted from the intercepts on the high-frequency axis and the semicircle in the high frequency region, respectively. The corresponding R_s and R_{ct} values can be obtained by fitting the

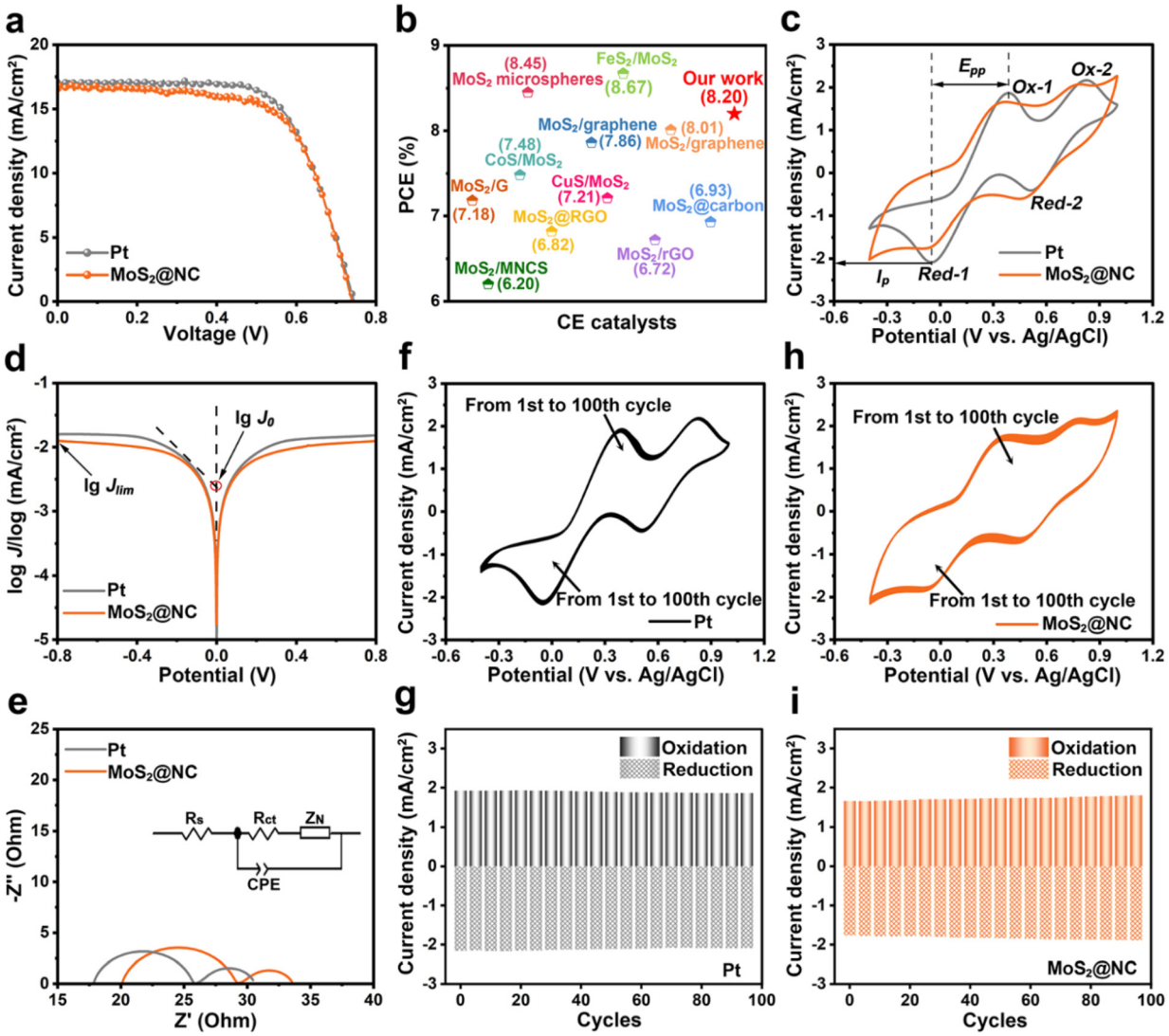

Fig. 4 (a) *J*–*V* curves of DSSCs fabricated with MoS_2@NC and Pt CEs. (b) A comparison of the PCE of MoS_2@NC with those of reported MoS_2-based CE catalysts. (c) CV curves at 50 mV s^{-1}, (d) Tafel polarization curves, and (e) Nyquist plots based on Pt and MoS_2@NC CEs. 100 consecutive CV curves at 50 mV s^{-1} and the corresponding anodic and cathodic peak current density *versus* cycles for (f and g) Pt and (h and i) MoS_2@NC.

Nyquist plots using an equivalent circuit and are listed in Table S4.† The R_s values reflect the adhesion between the CE catalyst and the FTO conductive substrate, while the R_{ct} values signify the charge transfer capability between the CE and the I_3^-/I^- redox couple in the electrolyte. As depicted in Fig. 4e and S8d,† both R_s and R_{ct} values follow the increasing trend: Pt (R_s = 17.78 Ω and R_{ct} = 7. 87 Ω), MoS_2@NC (R_s = 20.02 Ω and R_{ct} = 8.99 Ω), MoS_2@NC-1 (R_s = 20.49 Ω and R_{ct} = 10.14 Ω), and MoS_2@NC-3 (R_s = 21.07 Ω and R_{ct} = 13.20 Ω), suggesting that the optimized MoS_2@NC has superior charge transfer capability. Finally, the stability of Pt (Fig. 4f) and MoS_2@NC (Fig. 4h) electrodes were evaluated using consecutive CV curves. After 100 continuous scans, both Pt (Fig. 4g) and MoS_2@NC (Fig. 4i) exhibited no significant current change, implying their excellent stability. Moreover, MoS_2@NC-1 and MoS_2@NC-3 also showed remarkable stability (Fig. S9†). In conclusion, the as-synthesized MoS_2@NC demonstrates excellent catalytic activity and promising stability, showcasing its potential as a non-Pt alternative for efficient DSSCs.

3.4 DFT calculations for unveiling the mechanism

As previously mentioned, the designed MoS_2@NC demonstrated excellent catalytic activity for both the HER and IRR, highlighting its great potential as a bifunctional Pt-free catalyst. To gain deeper insights into the catalytic mechanism of MoS_2@NC for both the HER and IRR, the density functional theory (DFT) calculation was applied. Usually, constructing an appropriate model is crucial for revealing the catalytic mechanism. Although the above experimental results have proved that the obtained MoS_2@NC composites consist of 1T MoS_2, 2H MoS_2, and NC, taking this as a model will significantly increase the theoretical calculation amount. Therefore, a sim-

plified 2H MoS_2 (002)/NC model was constructed to minimize computational efforts and uncover the catalytic mechanism, which is effective in establishing a relationship between the structure and performance. The work function (φ) of MoS_2@NC and MoS_2 was initially considered, with the corresponding optimized models inserted in Fig. 5a and b, respectively. The φ value can be determined by the energy difference between the electrostatic potential and the Fermi level. Compared with MoS_2 (φ = 5.727 eV), MoS_2@NC exhibits a lower φ value of 4.840 eV, enhancing the charge transfer capability from the catalyst surface to the reactant molecule, which is conducive for accelerating the subsequent HER/IRR reaction kinetics.

For the HER, the water adsorption energy (E_{H_2O}) of the catalyst acts as an important indicator for estimating its activity. A suitable E_{H_2O} can effectively facilitate the adsorption and desorption of H_2O molecules, promoting efficient HER kinetics. The E_{H_2O} values of MoS_2@NC and MoS_2 are −0.194 and −0.141 eV (Fig. 5c), respectively, meaning that the water adsorption ability was further enhanced by constructing MoS_2@NC. Then, the Gibbs free energy (ΔG) of MoS_2@NC and MoS_2 during HER processes were calculated to provide insights into the

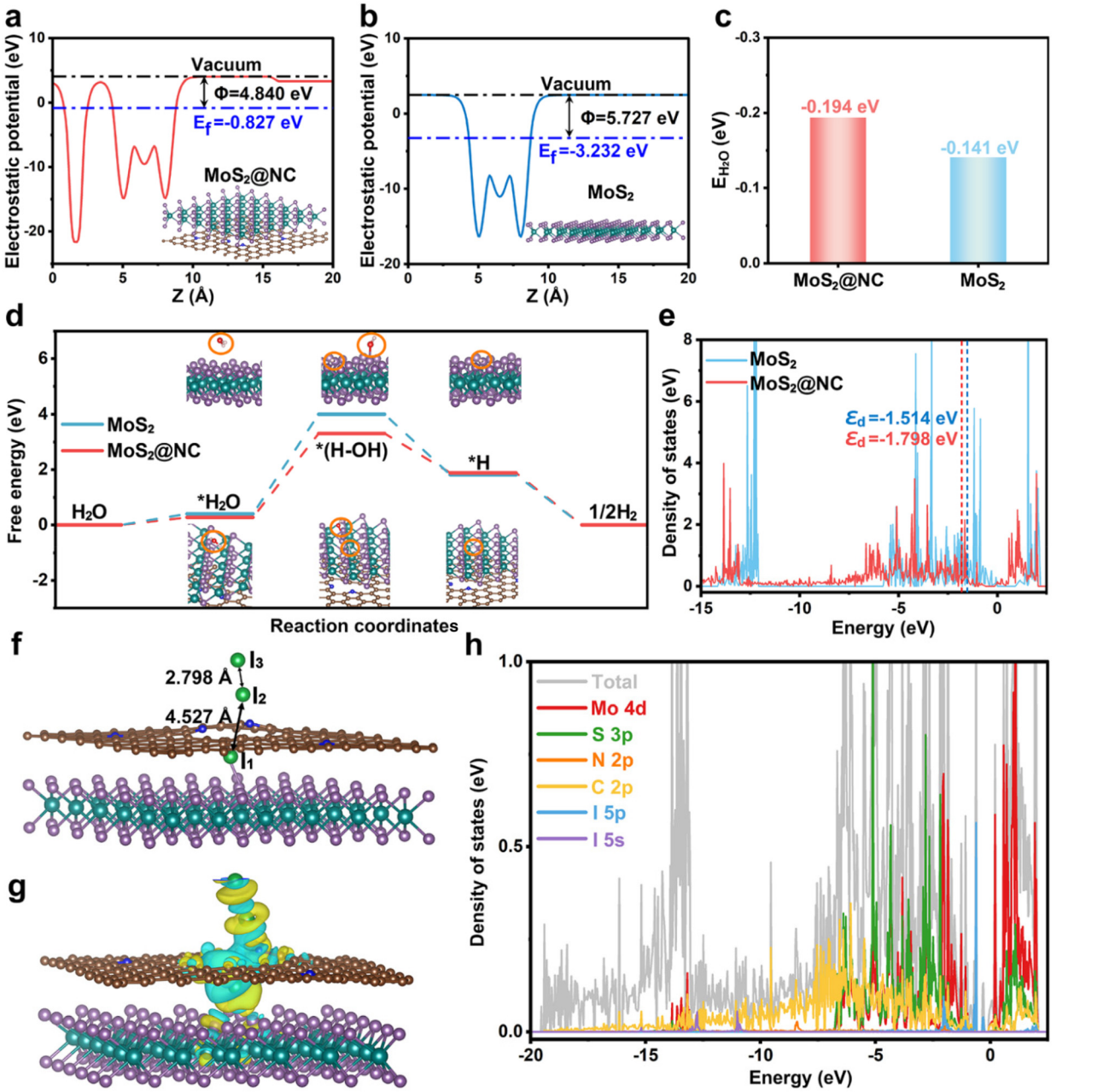

Fig. 5 The work function map and the corresponding model of (a) MoS_2@NC and (b) MoS_2. (c) E_{H_2O}, (d) Gibbs free energy diagram, and (e) DOSs of MoS_2@NC and MoS_2 during the HER process. (f) The adsorption configuration of I_3^-, (g) CDD, and (h) DOSs of MoS_2@NC during the IRR process.

reaction thermodynamics and help explain the variations in the catalytic activity; the corresponding adsorption models for H_2O, H_2O dissociation intermediates, and H* are inserted in Fig. 5d. It is obvious that the rate-determining rate step (RDS) in both catalysts is the dissociation of H_2O into *(H–OH). MoS_2@NC requires 3.037 eV to complete the RDS step, whereas MoS_2 demands 3.603 eV for the same process. This indicates that MoS_2@NC has a lower energy barrier for the RDS, highlighting its superior ability to facilitate the HER. Correspondingly, the charge density difference (CDD) of MoS_2@NC and MoS_2 before and after the RDS step further confirmed that the Mo site plays a major role in water dissociation (Fig. S10†). Compared to pure MoS_2 (−1.514 eV), the d-band center (ε_d) of MoS_2@NC shifted negatively to −1.798 eV (Fig. 5e), demonstrating enhanced *H adsorption energy after the construction of MoS_2@NC composites. Thus, MoS_2@NC exhibited superior HER activity compared to MoS_2.

In IRR, the primary role of the CE catalyst is characterized by its efficient reduction of I_3^- to I^-. A model of MoS_2@NC was established to elucidate the catalytic mechanism. As shown in Fig. 5f, I_3^- preferentially adsorbs at the interfacial S sites in MoS_2@NC. Correspondingly, the I_1–I_2 bond of I_3^- elongated from 2.95 Å to 4.527 Å, while the I_2–I_3 bond changed to 2.798 Å, implying that the interfacial S sites act as mainly active sites for IRR. The CDD of I_3^- on the interfacial S site was also calculated and depicted in Fig. 5g. It not only proves the formation of a covalent bond between the S site and I_1 of I_3^-, but also discloses the accumulation of electron density around the S–I_1 bond, along with a depletion of electron density around the I_2–I_3 bond, thus facilitating I_3^- reduction. To further explore the interaction between MoS_2@NC and I_3^-, the density of states (DOSs) was calculated (Fig. 5h). It was revealed that the interaction between the active sites of Mo 4d, S 3p, N 2p and I 5p facilitates the IRR process, showing a multi-site synergistic interaction mechanism. As a result, the aforementioned findings demonstrated that the positive synergistic effect between MoS_2 and NC endows MoS_2@NC with superior IRR activity.

4. Conclusions

In summary, we elaborately constructed a dodecahedron-like (1T, 2H) MoS_2@N-doped carbon composite (denoted as MoS_2@NC) catalyst by a four-step synthesis method, including coprecipitation, carbonization, acid washing, and the hydrothermal method. The characterization results not only proved that the as-prepared MoS_2@NC is composed of 1T-MoS_2, 2H-MoS_2 and NC, but also demonstrated the availability of edge active sites from small-sized (1T, 2H) MoS_2 nanosheets on the NC dodecahedron surface. The positive synergy between chemical components and structural advantages enables MoS_2@NC to show remarkable catalytic activity for both the HER and IRR. In the case of the HER, MoS_2@NC demonstrates impressive overpotentials at various current densities in 1.0 M KOH, significantly outperforming its counterparts and the most reported MoS_2-based HER catalyst. For the IRR, it was found that MoS_2@NC has Pt-like activity in iodine-based electrolytes, offering promising photovoltaic performance and excellent stability. Both HER and IRR results highlight the potential of MoS_2@NC as a bifunctional catalyst, implying its ability to replace Pt. DFT calculations revealed that the accelerated HER kinetics of MoS_2@NC mainly stem from the further enhanced E_{H_2O} and a lower energy barrier for overcoming the RDS step, while the improved IRR activity is primarily attributed to the interfacial S site in MoS_2@NC. In addition to developing an advanced HER/IRR bifunctional catalyst, this study provides systematic theoretical guidance and comprehensive insights into the design of highly active catalysts.

Data availability

All data that support the findings of this study are provided in the manuscript.

Conflicts of interest

The authors declare that there are no competing interests.

Acknowledgements

We gratefully acknowledge the support from the National Natural Science Foundation of China (22005161), the Fundamental Research Funds in Heilongjiang Provincial Universities of China (145309204), and the College Students' Innovative Entrepreneurial Training Plan Program (S202410232134).

References

1 N. S. Lewis, Research opportunities to advance solar energy utilization, *Science*, 2016, **351**, 6271.
2 Y.-Q. Jiao, H.-J. Yan, C.-G. Tian and H.-G. Fu, Structure engineering and electronic modulation of transition metal interstitial compounds for electrocatalytic water splitting, *Acc. Mater. Res.*, 2023, **4**, 42–56.
3 Q. Qian, Y. Zhu, N. Ahmad, Y. Feng, H. Zhang, M. Cheng, H. Liu, C. Xiao, G. Zhang and Y. Xie, Recent advancements in electrochemical hydrogen production via hybrid water splitting, *Adv. Mater.*, 2024, **36**, 2306108.
4 X. Wang, B. Zhao, W. Kan, Y. Xie and K. Pan, Review on low-cost counter electrode materials for dye-sensitized solar cells: Effective Strategy to improve photovoltaic performance, *Adv. Mater. Interfaces*, 2022, **9**, 2101229.
5 S. Yun, Z. Gao, T. Yang, M. Sun, G. Yang, K. Wang, Z. Wang, S. Yuan and M. Zhang, Constructing $NiSe_2$/$MoSe_2$ Mott–Schottky heterojunctions onto N-doped brain coral-carbon spheres by phase separation strategies for advanced

energy conversion applications, *Adv. Funct. Mater.*, 2024, **34**, 2314226.

6 X. Wang, Y. Zhang, C. Lv, Z. Liu, L. Wang, B. Zhao, T. Zhang, W. Xin and Y. Jiao, Colloid synthesis of $Ni_{12}P_5$/N, S-doped graphene as efficient bifunctional catalyst for alkaline hydrogen evolution and triiodide reduction reaction, *J. Colloid Interface Sci.*, 2023, **652**, 12–22.

7 D. Qiao, S. Yun, M. Sun, J. Dang, Y. Zhang, S. Yuan, G. Yang, T. Yang, Z. Gao and Z. Wang, 1D/3D trepang-like N-modified carbon confined bimetal carbides and metal cobalt: Boosting electron transfer via dual Mott-Schottky heterojunctions triggered built-in electric fields for efficient hydrogen evolution and tri-iodide reduction, *Appl. Catal., B*, 2023, **334**, 122830.

8 C. Lv, T. Zhang, X. Wang, H. Pan, Z. Xie, H. Lu, K. Pan and Y. Xie, Enhancement of the triiodide reduction reaction by doping molybdenum in NiSe hierarchical microspheres: a theoretical and experimental study, *Inorg. Chem. Front.*, 2023, **10**, 460–467.

9 Z. W. Seh, J. Kibsgaard, C. F. Dickens, I. Chorkendorff, J. K. Nørskov and T. F. Jaramillo, Combining theory and experiment in electrocatalysis: Insights into materials design, *Science*, 2017, **355**, eaad4998.

10 T. Wu, M. Sun, H. H. Wong, C. H. Chan, L. Lu, Q. Lu, B. Chen and B. Huang, Recent advances and strategies of electrocatalysts for large current density industrial hydrogen evolution reaction, *Inorg. Chem. Front.*, 2023, **10**, 4632–4649.

11 L. Quan, H. Jiang, G. Mei, Y. Sun and B. You, Bifunctional electrocatalysts for overall and hybrid water splitting, *Chem. Rev.*, 2024, **124**, 3694–3812.

12 J. Ding, Z. Peng, Z. Wang, C. Zeng, Y. Feng, M. Yang, G. Hu, J. Luo and X. Liu, Phosphorus-tungsten dual-doping boosts acidic overall seawater splitting performance over RuO_x nanocrystals, *J. Mater. Chem. A*, 2024, **12**, 28023–28031.

13 C. Lv, Y. Jing, Z. Lu, X. Wang, K. Zhu, J. Yin, Y. Xie and K. Ye, Manipulating electron redistribution in small-sized NiCoP colloidal nanocrystals for enhanced alkaline water/seawater electrolysis, *Chem. Eng. J.*, 2025, **510**, 161709.

14 X. Wang, T. Su, Z. Lu, L. Yu, N. Sha, C. Lv, Y. Xie and K. Ye, Morphological engineering of monodispersed Co_2P nanocrystals for efficient alkaline water and seawater splitting, *J. Colloid Interface Sci.*, 2025, **691**, 137389.

15 M. Yang, J. Ding, Z. Wang, J. Zhang, Z. Peng and X. Liu, NiMo-based alloy and its sulfides for energy-saving hydrogen production via sulfion oxidation assisted alkaline seawater splitting, *Chin. Chem. Lett.*, 2025, DOI: **10.1016/j.cclet.2025.110861**.

16 W. Liu, M. Zhou, J. Zhang, W. Liu, D. Qin, Q. Liu, G. Hu and X. Liu, Construction of a CoP/MnP/Cu_3P heterojunction for efficient methanol oxidation-assisted seawater splitting, *Mater. Chem. Front.*, 2025, **9**, 953–964.

17 H. Lu, J. Tournet, K. Dastafkan, Y. Liu, Y. H. Ng, S. K. Karuturi, C. Zhao and Z. Yin, Noble-metal-free multicomponent nanointegration for sustainable energy conversion, *Chem. Rev.*, 2021, **121**, 10271–10366.

18 W. Zhang, H. Yan, Y. Liu, D. Wang, Y. Jiao, A. Wu, X. Wang, R. Wang and C. Tian, Multi-interfacial engineering of an interlinked Ni_2P-MoP heterojunction to modulate the electronic structure for efficient overall water splitting, *J. Mater. Chem. A*, 2023, **11**, 15033–15043.

19 A. Ahmad, A. Nairan, Z. Feng, R. Zheng, Y. Bai, U. Khan and J. Gao, Unlocking the potential of high entropy alloys in electrochemical water splitting: A review, *Small*, 2024, **20**, 2311929.

20 X. Wang, N. Sha, N. Zhao, T. Su, C. Lv, L. Yang, Y. Xie and K. Ye, Structure engineering and surface reconstruction enabling MoNi hollow nanocube for efficient urea-assisted water electrolysis, *Chem. Eng. J.*, 2024, **499**, 156119.

21 Z. Shi, X. Zhang, X. Lin, G. Liu, C. Ling, S. Xi, B. Chen, Y. Ge, C. Tan, Z. Lai, Z. Huang, X. Ruan, L. Zhai, L. Li, Z. Li, X. Wang, G.-H. Nam, J. Liu, Q. He, Z. Guan, J. Wang, C.-S. Lee, A. R. J. Kucernak and H. Zhang, Phase-dependent growth of Pt on MoS_2 for highly efficient H_2 evolution, *Nature*, 2023, **621**, 300–305.

22 M. Acerce, D. Voiry and M. Chhowalla, Metallic 1T phase MoS_2 nanosheets as supercapacitor electrode materials, *Nat. Nanotechnol.*, 2015, **10**, 313–318.

23 S. Mahato, P. Nandigana, B. Pradhan, B. Subramanian and S. K. Panda, Enhanced efficiency of DSSC by lyophilized tin-doped molybdenum sulfide as counter electrode, *J. Alloys Compd.*, 2022, **894**, 162406.

24 H.-J. Liu, S. Zhang, Y.-M. Chai and B. Dong, Ligand modulation of active sites to promote cobalt-doped 1T-MoS_2 electrocatalytic hydrogen evolution in alkaline media, *Angew. Chem., Int. Ed.*, 2023, **62**, e202313845.

25 S. Tian, W. Chen, R. Wang, C. Qin, Z.-J. Jiang and Z. Jiang, Ar/NH_3 radio-frequency plasma etching and N-doping to stabilize metallic phase 1T-MoS_2 for fast and durable sodium-ion storage, *Adv. Funct. Mater.*, 2024, **34**, 2408035.

26 G. Wang, G. Zhang, X. Ke, X. Chen, X. Chen, Y. Wang, G. Huang, J. Dong, S. Chu and M. Sui, Direct synthesis of stable 1T-MoS_2 doped with Ni single atoms for water splitting in alkaline media, *Small*, 2022, **18**, 2107238.

27 B. Vedhanarayanan, J. Shi, J.-Y. Lin, S. Yun and T.-W. Lin, Enhanced activity and stability of MoS_2 through enriching 1T-phase by covalent functionalization for energy conversion applications, *Chem. Eng. J.*, 2021, **403**, 126318.

28 X. Zhang, P. Yang and S. P. Jiang, Ni diffusion in vertical growth of MoS_2 nanosheets on carbon nanotubes towards highly efficient hydrogen evolution, *Carbon*, 2021, **175**, 176–186.

29 T. F. Jaramillo, K. P. Jørgensen, J. Bonde, J. H. Nielsen, S. Horch and I. Chorkendorff, Identification of active edge sites for electrochemical H_2 evolution from MoS_2 nanocatalysts, *Science*, 2007, **317**, 100–102.

30 W. Li, Z. Sun, R. Ge, J. Li, Y. Li, J. M. Cairney, R. Zheng, Y. Li, S. Li, Q. Li and B. Liu, Nanoarchitectonics of La-doped Ni_3S_2/MoS_2 hetetostructural electrocatalysts for water electrolysis, *Small Struct.*, 2023, **4**, 2300175.

31 Y. Gao, J. Li, H. Gong, C. Zhang, H. Fan, X. Xie, X. Huang, H. Xue, T. Wang and J. He, The identified intrinsic active

sites for efficient and stable bi-functional catalyst N-MoS_2·Ni_3S_2/NiS: the Mo-N structure and Ni-S structure on the heterogeneous interface synergistically enhance water splitting, *J. Mater. Chem. A*, 2022, **10**, 11755–11765.

32 L. Fan, Y. Gong, J. Wan, Y. Wei, H. Shi and C. Liu, Flower-like molybdenum disulfide decorated ZIF-8-derived nitrogen-doped dodecahedral carbon for electro-catalytic degradation of phenol, *Chemosphere*, 2022, **298**, 134315.

33 J. P. Masnica, S. Sibt-e-Hassan, S. Potgieter-Vermaak, Y. N. Regmi, L. A. King and L. Tosheva, ZIF-8-derived Fe-C catalysts: Relationship between structure and catalytic activity toward the oxygen reduction reaction, *Green Carbon*, 2023, **1**, 160–169.

34 Q. Yan, Y. Liu, Y. Zhao, X. Zhou and W. Yuan, Molten salt-mediated electrosynthesis of MoS_2 nanosheet-supported Rh nanoclusters for highly efficient electrocatalytic hydrogen evolution, *Chem. Commun.*, 2025, **61**, 3700–3703.

35 Y. Cao, P. Yu, L. Wang, X. Wang, L. Li, M. Yu, C. Sun, Z. Liu and B. Zhao, Edge-active enriched MoS_2 porous nanosheets as efficient Pt-free catalysts toward the triiodide reduction reaction, *ACS Appl. Electron. Mater.*, 2023, **5**, 429–439.

36 X. Hou, H. Zhou, M. Zhao, Y. Cai and Q. Wei, MoS_2 nanoplates embedded in Co-N-doped carbon nanocages as efficient catalyst for HER and OER, *ACS Sustainable Chem. Eng.*, 2020, **8**, 5724–5733.

37 X. Wang, Z. Lu, Y. Cao, T. Su, L. Yu, J. Sun, B. Zhao, C. Lv and Y. Xie, Multi-synergy enabling Ni-doped MoS_2@N-doped carbon composite as versatile catalysts toward hydrogen production and photovoltaics, *Carbon*, 2025, **231**, 119724.

38 X. Geng, W. Sun, W. Wu, B. Chen, A. Al-Hilo, M. Benamara, H. Zhu, F. Watanabe, J. Cui and T.-P. Chen, Pure and stable metallic phase molybdenum disulfide nanosheets for hydrogen evolution reaction, *Nat. Commun.*, 2016, **7**, 10672.

39 X. Wang, Y. Xie, Y. Jiao, K. Pan, B. Bateer, J. Wu and H. Fu, Carbon nanotubes in situ embedded with NiS nanocrystals outperform Pt in dye-sensitized solar cells: interface improved activity, *J. Mater. Chem. A*, 2019, **7**, 10405–10411.

40 J. Yang, Y. Niu, J. Huang, L. Liu and X. Qian, N-doped C/$CoSe_2$@Co–$FeSe_2$ yolk-shell nano polyhedron as superior counter electrode catalyst for high-efficiency Pt-free dye-sensitized solar cell, *Electrochim. Acta*, 2020, **330**, 135333.

41 J. Li, J. Zheng, C. Wu, H. Zhang, T. Jin, F. Wang, Q. Li and E. Shangguan, Facile synthesis of Fe_3S_4 microspheres as advanced anode materials for alkaline iron-based rechargeable batteries, *J. Alloys Compd.*, 2021, **874**, 159873.

42 K. Li, D. Feng and Y. Tong, Hierarchical metal sulfides heterostructure as superior bifunctional electrode for overall water splitting, *ChemSusChem*, 2022, **15**, e202200590.

43 H. Cheng, F. Yi, A. Gao, H. Liang, D. Shu, X. Zhou, C. He and Z. Zhu, Supermolecule self-assembly promoted porous N, P Co-doped reduced graphene oxide for high energy density supercapacitors, *ACS Appl. Energy Mater.*, 2019, **2**, 4084–4091.

44 Z. Nie, Y. Wang, X. Li, R. Wang, Y. Zhao, H. Song and H. Wang, Heteroatom-doped hierarchical porous carbon from corn straw for high-performance supercapacitor, *J. Energy Storage*, 2021, **44**, 103410.

45 L. Zhang, J. Xiong, Y.-H. Qin and C.-W. Wang, Porous N-C catalyst synthesized by pyrolyzing g-C_3N_4 embedded in carbon as highly efficient oxygen reduction electrocatalysts for primary Zn-air battery, *Carbon*, 2019, **150**, 475–484.

46 S. Huang, Y. Meng, S. He, A. Goswami, Q. Wu, J. Li, S. Tong, T. Asefa and M. Wu, N-, O-, and S-tridoped carbon-encapsulated Co_9S_8 nanomaterials: Efficient bifunctional electrocatalysts for overall water splitting, *Adv. Funct. Mater.*, 2017, **27**, 1606585.

47 Z. Lu, Y. Cao, J. Xie, J. Hu, K. Wang and D. Jia, Construction of Co_2P/CoP@Co@NCNT rich-interface to synergistically promote overall water splitting, *Chem. Eng. J.*, 2022, **430**, 132877.

48 K. Ding, W. Wang, D. Yu, W. Wang, P. Gao and B. Liu, Facile formation of flexible Ag/AgCl/polydopamine/cotton fabric composite photocatalysts as an efficient visible-light photocatalysts, *Appl. Surf. Sci.*, 2018, **454**, 101–111.

49 D. Pang, C.-C. Wang, P. Wang, W. Liu, H. Fu and C. Zhao, Superior removal of inorganic and organic arsenic pollutants from water with MIL-88A(Fe) decorated on cotton fibers, *Chemosphere*, 2020, **254**, 126829.

50 K. Ao and W. A. Daoud, Facile controlled formation of CoNi alloy and CoO embedded in N-doped carbon as advanced electrocatalysts for oxygen evolution and zinc-air battery, *Electrochim. Acta*, 2021, **395**, 139204.

51 J. Dong, X. Zhang, J. Huang, J. Hu, Z. Chen and Y. Lai, *In situ* formation of unsaturated defect sites on converted CoNi alloy/Co-Ni LDH to activate MoS_2 nanosheets for pH-universal hydrogen evolution reaction, *Chem. Eng. J.*, 2021, **412**, 128556.

52 L. Yang, X. Yuan, C. Chen, Q. Wang, W. Liang and R. Song, Rational design of MoS_2@M (M=Sn, Cu, Ni, Co) hybrid nanostructures for enhanced electrocatalytic hydrogen evolution reaction, *Mater. Chem. Phys.*, 2024, **318**, 129234.

53 A. Wu, Y. Gu, Y. Xie, H. Yan, Y. Jiao, D. Wang and C. Tian, Interfacial engineering of MoS_2/MoN heterostructures as efficient electrocatalyst for pH-universal hydrogen evolution reaction, *J. Alloys Compd.*, 2021, **867**, 159066.

54 H. Zhao, M. Liu, X. Du and X. Zhang, Synthesis of M-NiS/Mo_2S_3 (M=Co, Fe, Ce and Bi) nanoarrays as efficient electrocatalytic hydrogen evolution reaction catalyst in fresh and seawater, *Int. J. Hydrogen Energy*, 2024, **62**, 532–540.

55 J. Xu, G. Shao, X. Tang, F. Lv, H. Xiang, C. Jing, S. Liu, S. Dai, Y. Li, J. Luo and Z. Zhou, Frenkel-defected monolayer MoS_2 catalysts for efficient hydrogen evolution, *Nat. Commun.*, 2022, **13**, 2193.

56 P. S. Venkatesh, N. Kannan, M. G. Babu, G. Paulraj and K. Jeganathan, Transition metal doped MoS_2 nanosheets for electrocatalytic hydrogen evolution reaction, *Int. J. Hydrogen Energy*, 2022, **47**, 37256–37263.

57 M. K. Kim, B. Lamichhane, B. Song, S. Kwon, B. Wang, S. Kattel, J. H. Lee and H. M. Jeong, Enhancing electro-

catalytic hydrogen evolution of MoS_2 enabled by electrochemical cation implantation for simultaneous surface-defect and phase engineering, *Appl. Catal. B: Environ. Energy*, 2024, **352**, 124037.

58 N. A. Khan, G. Rahman, S. Y. Chae, A. U. H. A. Shah, O. S. Joo, S. A. Mian and A. Hussain, Boosting electrocatalytic hydrogen generation from water splitting with heterostructured $MoS_2/NiFe_2O_4$ composite in alkaline media, *Int. J. Hydrogen Energy*, 2024, **69**, 261–271.

59 K. S. Chandrakantha, Z. Zuo, B. N. Chandrashekar, A. Amini, K. S. Rangappa, S. Srikantaswamy and C. Cheng, Synergistic effects of 1T-2H MoS_2 and laser-reduced graphene oxide-ZnO scaffold composite catalyst for efficient hydrogen evolution reaction, *Mater. Today Energy*, 2024, **45**, 101683.

60 S. C. Pathan, J. S. Shaikh, N. S. Shaikh, V. Márquez, M. Rittiruam, T. Saelee, P. Khajondetchairit, S. S. Mali, J. V. Patil, C. K. Hong, P. Praserthdam and S. Praserthdam, Electrocatalytic overall water splitting based on $(ZnNiCoFeY)_xO_y$ high-entropy oxide supported on MoS_2, *S. Afr. J. Chem. Eng.*, 2024, **48**, 425–435.

61 Y.-N. Zhao, N. Sun, S. Xu, S. Min, H. Dong, J. Li, C. Liu and Z. Chen, An interface engineering strategy of MoS_2/perovskite oxide as a bifunctional catalyst to boost overall water splitting, *J. Mater. Chem. A*, 2024, **12**, 8757–8768.

62 Y. Zhang, H. Zhou, H. Wang, Y. Zhang and D. D. Dionysiou, Synergistic effect of reduced graphene oxide and near-infrared light on MoS_2-mediated electrocatalytic hydrogen evolution, *Chem. Eng. J.*, 2021, **418**, 129343.

63 G. Zhu, H. Xu, H. Wang, W. Wang, Q. Zhang, L. Zhang and H. Sun, Microwave assisted synthesis of MoS_2/nitrogen-doped carbon shell-core microspheres for Pt-free dye-sensitized solar cells, *RSC Adv.*, 2017, **7**, 13433–13437.

64 B. Pang, Y. Shi, S. Lin, Y. Chen, J. Feng, H. Dong, H. Yang, Z. Zhao, L. Yu and L. Dong, Triiodide reduction activity of hydrangea molybdenum sulfide/reduced graphene oxide composite for dye-sensitized solar cells, *Mater. Res. Bull.*, 2019, **117**, 78–83.

65 X. Yuan, X. Li, X. Zhang, Y. Li and L. Liu, MoS_2 vertically grown on graphene with efficient electrocatalytic activity in Pt-free dye-sensitized solar cells, *J. Alloys Compd.*, 2018, **731**, 685–692.

66 K. Zhang, J. Yao, Q. Yang, X. Zuo, H. Tang, F. Du, G. Li and W. Wang, Cotton shells -like floriform molybdenum disulfide@carbon electrocatalyst for high performance dye-sensitized solar cells, *Sol. Energy*, 2017, **157**, 948–955.

67 S. Jiang, X. Yin, J. Zhang, X. Zhu, J. Li and M. He, Vertical ultrathin MoS_2 nanosheets on a flexible substrate as an efficient counter electrode for dye-sensitized solar cells, *Nanoscale*, 2015, **7**, 10459–10464.

68 S. Hussain, S. A. Patil, A. A. Memon, D. Vikraman, B. A. Naqvi, S. H. Jeong, H.-S. Kim, H.-S. Kim and J. Jung, CuS/WS_2 and CuS/MoS_2 heterostructures for high performance counter electrodes in dye-sensitized solar cells, *Sol. Energy*, 2018, **171**, 122–129.

69 X. Wang, Y. Xie, Z. Cai, N. Xiong, Z. Xu, M. Li, Q. Feng, W. Zhou and K. Pan, The sesame ball-like CoS/MoS_2 nanospheres as efficient counter electrode catalysts for dye-sensitized solar cells, *J. Alloys Compd.*, 2018, **739**, 568–576.

70 J. Ma, W. Shen and F. Yu, Graphene-enhanced three-dimensional structures of MoS_2 nanosheets as a counter electrode for Pt-free efficient dye-sensitized solar cells, *J. Power Sources*, 2017, **351**, 58–66.

71 S. Li, H. Min, F. Xu, L. Tong, J. Chen, C. Zhu and L. Sun, All electrochemical fabrication of MoS_2/graphene counter electrodes for efficient dye-sensitized solar cells, *RSC Adv.*, 2016, **6**, 34546–34552.

